JZUS

Damage behavior of steel beam-to-column connections under inelastic cyclic loading[*]

Xi-yue LIU[1,2], Yuan-qing WANG[†‡2], Jun XIONG[3], Yong-jiu SHI[2]

(*1College of Basic Education for Commanding Officers, National University of Defense Technology, Changsha 410072, China*)

(*2Key Laboratory of Civil Engineering Safety and Durability of China Education Ministry, Department of Civil Engineering, Tsinghua University, Beijing 100084, China*)

(*3Nanjing Jianye District Bureau of Construction and Transport, Nanjing 210019, China*)

[†]E-mail: wang-yq@mail.tsinghua.edu.cn

Abstract: Brittle cracks were observed in the welded beam-to-column connections of steel frames during an earthquake. The crack propagation and accumulated damage to the connections can lead to fractures at much lower ductility ratios. Understanding the connections' damage behavior during an earthquake is crucial for the design of steel moment frames in seismic areas. Nine full scale beam-to-column connections were tested under constant amplitude and variable amplitude cyclic loading. The effects of loading amplitude, loading history, and peak load on the connection damage were analyzed. The damage characters were studied and three damage evolution models were calibrated and validated based on test results. The damage mechanism was investigated and an effective plastic strain index was developed to evaluate connection damage based on a ductile fracture mechanism. A fatigue fracture mechanics-based model, for evaluating the damage process of beam-to-column connections under cyclic loading, was proposed.

Key words: Beam-to-column connection; Cyclic loading; Connection test; Damage mechanism; Ductile fracture
http://dx.doi.org/10.1631/jzus.A1600520   **CLC number:** TH161.12

1 Introduction

Modern earthquake resistant design relies on structural ductility to absorb seismic energy, which requires that a structure has large inelastic deformability for the dissipation of seismic energy. It had been assumed that steel moment connections were able to deform plastically to large rotations, absorbing significant amounts of energy, until the 1994 Northridge earthquake (Toyoda, 2002) and the 1995 Kobe earthquake (Kuwamura, 1998). Inspection after these severe earthquakes revealed that a large number of connections had suffered brittle fractures in steel moment resisting frames (SMRFs). Brittle cracks were observed in the welded beam-to-column connections of SMRFs, and the connections fractured at much lower ductility ratios (Sakano and Wahab, 2001; Chen, 2007; Saiprasertkit *et al.*, 2012). This prompted several studies to investigate the seismic behavior of the welded connections, for example, the SAC steel project started by the Structural Engineers Association of California (SEAOC), the Applied Technology Council (ATC), and California Universities for Research in Earthquake Engineering (CUREE).

A considerable number of experiments were conducted worldwide, to investigate the performance of steel connections under cyclic loads (Fisher *et al.*, 1995; El-Tawil *et al.*, 1998; Su, 2005; Shi W.L. *et al.*,

2008; Shi Y.J. *et al.*, 2009). A series of monotonic tensile tests on T-stub welded specimens were carried out (Kuwamura and Yamamoto, 1997; Kuwamura and Takagi, 2004). The effects of weld fracture on the damage behavior of the connections were analyzed. The test results indicated that most brittle fractures initiate from welds; a weld's toughness has a significant influence on its ultimate deformation and cracking load. Tateishi and Hanji (2004) conducted ultralow cycle loading tests on structural steels and the corresponding weld metals to investigate the effects of strain amplitude on material fatigue, life and damage processes. A damage mechanics-based model to evaluate fatigue life of structural steel and heat-affected zone was also proposed. Most of these experiments were mainly focused on the effect of the welding technology used, or the material toughness or construction details of the connections fracture; however, they do not investigate deeply the character of the connection damages (Dexter and Melendrez, 2000; Anderson *et al.*, 2002; Chi and Uang, 2002; Wang and Chen, 2005). Only limited mechanical models for analyzing the behavior of connections have taken connection damage and deterioration processes into consideration at present (Nip *et al.*, 2010). Previous research showed that during severe earthquakes, connection damage was a key factor affecting frame strength and stability. The accumulated damage and crack propagation in welds or the heat affected zone of welded connections can lead to fractures at much lower ductility levels. An accurate understanding of the damage and deterioration of connections under earthquake conditions is crucial for the design of SMRFs in seismic areas.

Recently, more effort has been made to study connection damage and fractures under severe earthquake conditions. A damage model considering the crack effect, which was used for steel mechanical components and connections, was proposed (Shen and Shen, 2002). Shaking table tests on steel moment frames were implemented (Li *et al.*, 2004); the Park-Ang model was applied to analyze the steel moment frame damage and the model was validated by test results. However, in the field of seismic design for steel connections research is still mainly concerned with the stiffness and strength of connections; studies on the evolution of connections damage and hysteretic models that incorporate damage are limited.

Establishing a methodology to quantify connection damage is crucial for investigating the connection damage process. At present, material damage is always calibrated by test, based on the concept that material damage is in direct proportion to the decrease of strength when subjected to monotonic tensile load. However, the stress state in a connection is heterogeneous and complicated; the damage level varies at different locations. Therefore, the microscopic-based relationship between material damage and bearing capacity needs to be validated when applying the macro connection analysis, and the relationship between connection damage and the macro mechanic index needs to be established by further investigation for the connection damage model. Besides, the effects of loading history and loading amplitude on the connection damage are not considered by previous related work.

In this study, nine full scale beam-to-column connections were tested in which five connections were under variable amplitude (VA) cyclic loading and four were under constant amplitude (CA) cyclic loading. Subsequently, three existing damage evolution models were calibrated and validated based on the test results. A damage mechanism was introduced and an effective plastic strain index was developed to evaluate connection damage based on ductile fracture mechanism. Finally, a fatigue fracture mechanics-based model for evaluating the crack and damage processes of welded connections under cyclic loading was proposed.

2 Beam-to-column connection tests

2.1 Specimens and materials

Nine full scale beam-to-column connection specimens were designed and fabricated according to MOHURD (2003; 2010). These nine specimens represented the exterior beam-to-column connections in SMRFs. The total length of the beam was 1650 mm and the total height of the column was 2300 mm. Geometries of the connection specimens are shown in Fig. 1. A strong column-weak beam design philosophy was adopted to force plastic hinge formation at the beam end near the column face. The specimen consisted of a built-up welded H-shaped beam section H-400 mm×150 mm×8 mm×12 mm and a welded

H-shaped column section H-450 mm×250 mm× 12 mm×16 mm. The stiffness ratio of beam to column I_b/I_c is 0.42, and the width-thickness ratio of the plate meets the requirements of MOHURD (2003).

A welded-flange bolted-web detail was used in the connection, i.e., the beam flanges were welded to the column flanges with complete joint penetration (CJP) groove weld (Grade E50) with CO_2 gas metal arc welding procedure (GMAW), which is one of the common welding practices in constructions in China. The beam web was linked to the column by four pretensioned high strength bolts (Φ20 Gr. 10.9). The quality of beam flange to column flange welds achieved first class classification by ultrasonic test. Geometries of weld access holes (WAHs) and weld details around the top and bottom beam flange to column flange welds are shown in Fig. 1. The weld backing bars were left in place for all specimens and no fillet weld reinforcement was added beneath the backing bars.

All the specimens were fabricated from the common steel Q345 (nominal yield strength 345 MPa). The mechanical properties of the Q345 steel plates (with different plate thicknesses) used in the specimens were obtained by standard tensile coupon tests and are presented in Table 1.

Table 1 Mechanical properties of Q345 steel plates used in the test specimens

Thickness, t (mm)	Young's modules, E (GPa)	Yield strength, σ_y (MPa)	Ultimate tensile strength, σ_u (MPa)
8	208.1	354.5	481.3
12	206.1	359.9	524.7
16	204.1	393.0	547.3

2.2 Test setup, loading protocol, and measurement

The specimens were mounted to the strong floor and reaction wall. The schematic plot and general view of the test setup are shown in Fig. 2. Roller supports were provided at both ends of the column to ensure the column could deform freely under axial loading. One end of the column was fixed to the reaction wall, the other end was subjected to axial loads which were implemented by an actuator with a 1000 kN load capacity. In order to achieve the design philosophy of strong column-weak beam as
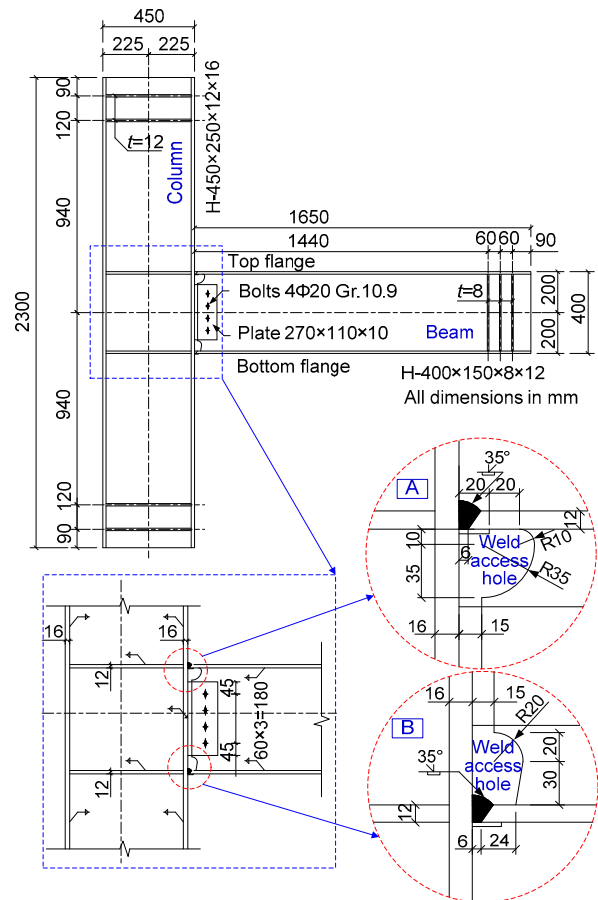

Fig. 1 Geometries and weld details of the beam-to-column connection specimen (unit: mm)

mentioned above, a small ratio of axial load to column bearing capacity was adopted to ensure the column ductility. The column section was preloaded with 500 kN, and the axial load ratio was controlled at 0.18 in this test. Another servo-controlled actuator, capable of applying loads up to 500 kN and displacements up to ±150 mm was employed to provide cyclic loads at the beam tip. Lateral braces were installed at the beam tip just below the actuator in order to prevent lateral buckling of the beam.

A predetermined cyclic loading protocol was applied to the beam tip of each connection to simulate seismic loading. As shown in Table 2, each specimen was assigned a different loading protocol in tests. Five specimens (i.e., S-1 to S-5) were tested quasi-statically under variable amplitude cyclic loading (load types denoted as VA-1 to VA-5), and four specimens (i.e., S-6 to S-9) were tested under CA cyclic loading (load types denoted as CA-1 to CA-4).

All the specimens except S-1 were loaded by displacement control, while specimen S-1 was loaded by a combination of force and displacement control.

As listed in the third column of Table 2, the cyclical loading sequences were subdivided by square brackets. Displacement amplitudes were specified in multiples of yielding displacement δ_y (which represents the displacement at the cantilever end when the maximum beam bending stress reaches its yield strength). The yielding displacement δ_y for all the specimens was 15 mm. The symbol Δ denotes the increment of force or displacement amplitude in a loading sequence (enclosed by a pair of square brackets). The specimens were subjected to two cycles within each increment of displacement amplitude.

2.3 Test measurement

Specimens were instrumented with a combination of displacement transducers, strain gauge rosettes,
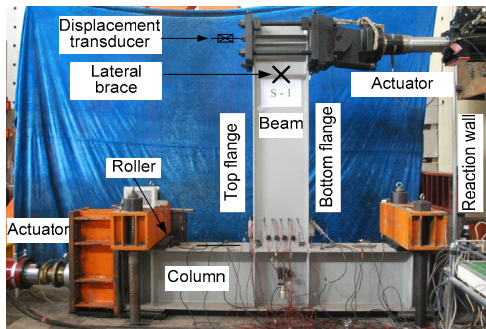

Fig. 2 General view of test setup, measurement, and specimen

Table 2 Loading histories adopted in the experiments

Specimen	Load type	Loading scheme
S-1	VA-1	$[(\pm 50 \text{ kN} \rightarrow \pm 150 \text{ kN}), \Delta=+50 \text{ kN}]$ $+[(\pm 1.25\delta_y \rightarrow \pm 2.25\delta_y), \Delta=+0.50\delta_y]$
S-2	VA-2	$[(\pm 0.25\delta_y \rightarrow \pm 2.25\delta_y), \Delta=+0.25\delta_y]$
S-3	VA-3	$[(\pm 0.25\delta_y \rightarrow \pm 1.50\delta_y), \Delta=+0.25\delta_y]$ $+[(\pm 1.50\delta_y \rightarrow \pm 1.00\delta_y), \Delta=-0.25\delta_y]$ $+[(\pm 1.00\delta_y \rightarrow \pm 2.25\delta_y), \Delta=+0.25\delta_y]$
S-4	VA-4	$[(\pm 0.25\delta_y \rightarrow \pm 2.00\delta_y), \Delta=+0.25\delta_y]$ $+[(\pm 2.00\delta_y \rightarrow \pm 1.00\delta_y), \Delta=-0.25\delta_y]$ $+[(\pm 1.00\delta_y \rightarrow \pm 2.25\delta_y), \Delta=+0.25\delta_y]$
S-5	VA-5	$[(\pm 0.25\delta_y \rightarrow \pm 1.00\delta_y), \Delta=+0.25\delta_y]$ $+[(\pm 2.00\delta_y \rightarrow \pm 1.00\delta_y), \Delta=-0.25\delta_y]$ $+[(\pm 1.00\delta_y \rightarrow \pm 2.00\delta_y), \Delta=+0.25\delta_y]$
S-6	CA-1	$CA=2.00\delta_y$
S-7	CA-2	$CA=1.75\delta_y$
S-8	CA-3	$CA=1.50\delta_y$
S-9	CA-4	$CA=1.25\delta_y$

and uniaxial strain gauges to measure global and local responses. Moment connections and deformation needed to be measured for the subsequent damage analysis of the connections. The connection rotation was obtained by measuring beam tip displacement, in accordance with the European code EC3-2005 (BS, 2005) and previous research (Shi W.L. *et al.*, 2008). As shown in Fig. 2, the displacement transducer was installed at beam loading point to measure the beam tip displacement. The rotation of the plastic connection was calculated by

$$\varphi = (\delta - \delta_e) / L, \tag{1}$$

where δ denotes the tested value of beam tip displacement, and δ_e denotes the beam's elastic deformation, $\delta_e=PL^3/(3EI)$, where L is the length of the beam, and I is the moment of inertia. The histories of beam tip load P and beam tip displacement δ of each specimen were directly measured. Five strain gauges were also attached to the beam flange surface, 100 mm away from the column flange.

3 Test results

3.1 Phenomenon

A summary of test phenomena for each specimen is given in Table 3. The beam tip load P_f and beam tip displacement δ_f correspond to the critical point of beam flange fracture. The number of cycles to fracture N_f and the total number of cycles to complete failure N_{total} were also recorded. Failure modes are briefly described in the last column of Table 3.

The test phenomena of the nine specimens are summarized as follows:

All the specimens had a similar failure process. For specimens S-4, S-6, and S-8, cracks initiated from the toe of the WAH at the top flange, and the cracks in the other specimens initiated from the toe of the WAH at the top flange. After initiation, cracks propagated progressively through the thickness of the beam flange. The toe of the WAH is defined as the region where the access hole transits into the beam flange (i.e., intersection of the WAH surface and the beam flange inner surface). When the crack went through the beam flange thickness and reached the micro

Table 3 Summary of test phenomena

Specimen	P_f (kN)	δ_f (mm)	N_f	N_{total}	Failure modes description
S-1	+263.30	+34.35	10.25	12 (6+6)[a]	N=10.25[c]: crack initiated from toe of WAH[d] at BF[e]; local buckling of TF[f]; N=10.75: crack grew through thickness of TF at the toe of WAH (50 mm along flange width)
	−185.13	−26.44	10.75		
S-2	+276.44	+33.24	16.25	18 (6+12)	N=16.25: crack propagated deep into BF at the toe of WAH (40 mm); N=16.75: crack grew through thickness of TF at the toe of WAH (40 mm); necking of TF edges
	−221.63	−25.78	16.75		
S-3	+245.11	+33.31	21.25	23 (6+17)	N=21.25: crack grew through thickness of BF at the toe of WAH (31 mm), local buckling of TF; N=21.75: crack propagated deep into TF at the toe of WAH
	−264.70	−33.27	21.75		
S-4	+264.91	+30.05	31.25	34 (6+28)	N=30.75: crack grew through thickness of TF at the toe of WAH (20 mm); N=31.25: crack propagated deep into BF at the toe of WAH
	−237.28	−29.98	30.75		
S-5	+214.20	+26.24	22.25	25 (6+19)	N=22.25: crack grew through thickness of BF at the toe of WAH (50 mm), propagated to 85 mm long in the next cycle; N=22.75: crack grew into TF at the toe of WAH
	−257.73	−26.30	22.75		
S-6	+261.55	+29.96	7.25	10[b]	N=5.75: crack grew through thickness of TF at the toe of WAH (25 mm), propagated to 50 mm long in the next cycle; N=7.25: crack grew into BF at the toe of WAH
	−250.02	−29.89	5.75		
S-7	+241.62	+26.29	9.25	13	N=9.25: crack grew through thickness of BF at the toe of WAH (40 mm), propagated to 80 mm in the next cycle; N=11.75: crack grew into TF at the toe of WAH
	−246.28	−26.20	11.75		
S-8	+253.00	+22.47	11.25	17	N=9.75: crack grew through thickness of TF at the toe of WAH (15 mm), propagated 10 mm long in each cycle; N=11.25: crack grew deep into BF at the toe of WAH
	−243.40	−22.50	9.75		
S-9	+213.57	+18.72	39.25	62	N=39.25: crack grew through thickness of BF at the toe of WAH; N=39.75: crack grew through thickness of TF at the toe of WAH, propagated to 17 mm long at N=42.75
	−212.98	−18.66	39.75		

[a] The expression in the parentheses denotes the number of elastic cycles plus plastic cycles; [b] All the cycles are in plastic; [c] N denotes the current cycles endured by the specimen (one cycle is divided into four quarters); [d] WAH is short for weld access hole; [e] BF is short for bottom flange of the beam; [f] TF is short for top flange of the beam

crack in the welds at the backing bar, the crack grew along the edge of weld backing bar, which led to the whole section fracture of the beam flange.

All cracks in the specimens initiated from the toe of the WAH, and the fracture positions were located at the top edge of weld backing bar. When the crack grew across the width of one beam flange, the crack at the other flange would stop propagating. All the specimens fractured at the beam flange accompanying with larger WAH except specimen S-7.

Some of the specimens were observed to have local buckling and necking of the beam flanges after crack initiations in the experiments.

3.2 Hysteretic curve

The hysteretic behavior of connection moment versus rotation curves are shown in Fig. 3. The shape of the hysteretic curves for each specimen seem to be symmetrical until three or four cycles before specimen failure, and the hysteretic curves become unsymmetrical when approaching failure.

3.3 Strength and ductility

The typical failure modes of the tested connection specimens are shown in Fig. 4.

The strength and the deformation capacity of each specimen are summarized in Table 4 (p.916), where the ultimate strength F_u denotes the maximum beam tip load over the whole loading history and δ_u is the corresponding beam tip displacement. M_u denotes the maximum moment applied to the specimen and φ_u is the corresponding connection plastic rotation. δ_{max} and φ_{max} denote the maximum beam tip displacement and the maximum connection rotation during the whole loading process, respectively. The positive or negative sign represents the half cycle within which the bottom flange or the top flange is in tension, respectively.

3.4 Connection stiffness

A bilinear model was adopted to calculate the specimen stiffness based on the connection skeleton curves, and the damage phase was not taken into
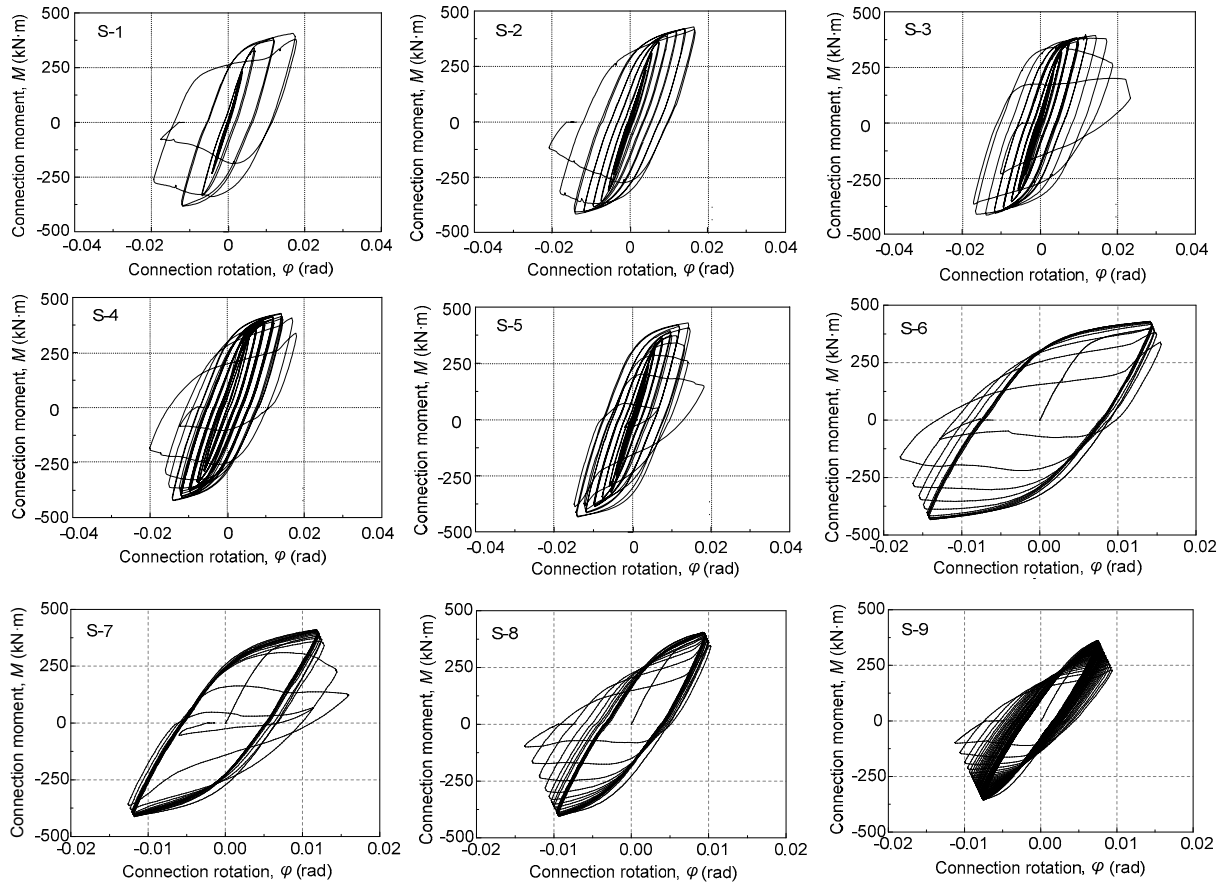
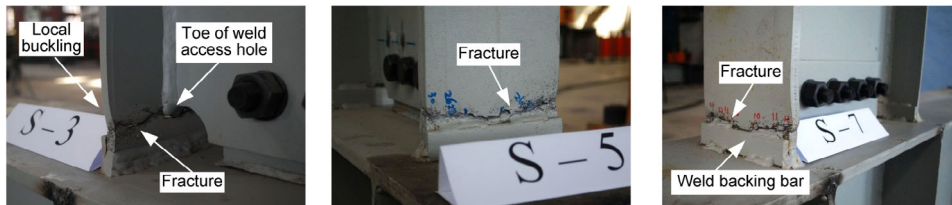**Fig. 3 Hysteretic curves of connection moment versus rotation**

Fig. 4 Typical failure modes of the test specimens (S-3, S-5, and S-7)

consideration. The yield points were obtained from the strain gauges attached to the beam flange edge. The value of the ultimate moment in the model was assumed to be the average value of those obtained at the tension cycle and the compression cycle, and this approach of assumption is also applied for the value of ultimate rotation in the model.

The parameter definition of this bilinear model is somewhat different from the European code. Fig. 5 shows the comparison between the simplified bilinear model and the European code model. $S_{j,\text{ini}}$ in the figure denotes the initial tangent rigidity of connection. The schematic of parameter calibrations for the

bilinear model is shown in Fig. 5b by taking specimen S-2 as an example. The stiffness values of each specimen are given in Table 5, where K_e denotes the elastic stiffness, and K_p is the hardening stiffness. The connection yield moment M_y, ultimate moment M_u, and their corresponding rotations φ_y, φ_u for the bilinear model are also listed in Table 5.

As listed in Table 5, for CA loaded connections S-6–S-9, the ductility coefficient φ_u/φ_y and hardening coefficient M_u/M_y all decreased with the decreasing loading amplitude. This shows that the deformation of the plastic connection becomes smaller under relatively small loading amplitudes.

Table 4 Loading capacity and deformation

Specimen	F_u (kN)	δ_u (mm)	M_u (kN·m)	φ_u (rad)	δ_{max} (mm)	φ_{max} (rad)
S-1	+271.1	+34.2	+406.6	+0.017	+34.7	+0.018
	−255.1	−25.8	−382.7	−0.012	−34.7	−0.019
S-2	+285.6	+33.6	+428.3	+0.016	+33.6	+0.017
	−276.0	−29.7	−414.0	−0.014	−33.6	−0.021
S-3	+265.4	+26.1	+398.1	+0.012	+37.3	+0.023
	−276.5	−29.7	−414.7	−0.014	−33.6	−0.017
S-4	+288.5	+30.2	+432.8	+0.014	+34.2	+0.018
	−285.1	−30.0	−427.7	−0.014	−34.1	−0.020
S-5	+287.6	+30.1	+431.4	+0.014	+30.3	+0.018
	−288.3	−30.2	−432.4	−0.014	−30.2	−0.015
S-6	+286.5	+30.3	+429.8	+0.014	+30.4	+0.016
	−288.8	−30.2	−433.3	−0.014	−30.3	−0.018
S-7	+273.7	+26.3	+410.6	+0.012	+26.5	+0.016
	−274.9	−26.5	−412.3	−0.012	−26.5	−0.013
S-8	+270.0	+22.4	+405.0	+0.009	+22.7	+0.010
	−270.0	−22.6	−405.0	−0.009	−22.7	−0.014
S-9	+240.7	+18.8	+361.1	+0.007	+18.9	+0.009
	−237.7	−18.9	−356.6	−0.008	−18.9	−0.011
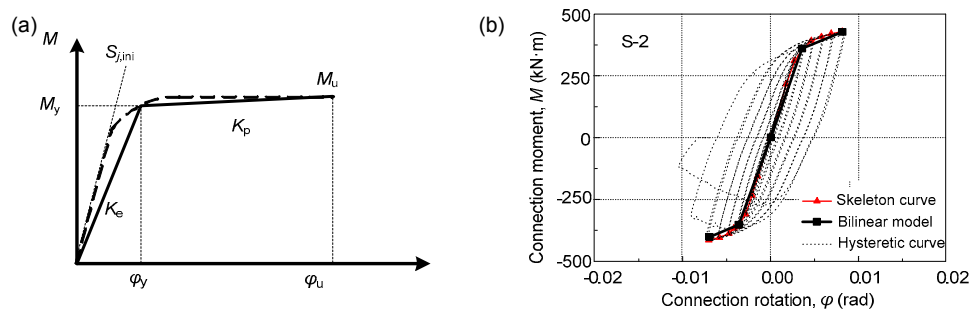
Fig. 5 Connection stiffness calculation

(a) Schematic of connection stiffness calculation; (b) Comparison between simplified stiffness curve and skeleton curve

Table 5 Stiffness of specimens

Specimen	φ_y (rad)	M_y (kN·m)	φ_u/φ_y	M_u/M_y	K_e (kN·m/rad)	$(K_{e(S-i)}-K_{e(S-2)})/K_{e(S-2)}$	K_p (kN·m/rad)	$(K_{p(S-i)}-K_{p(S-2)})/K_{p(S-2)}$
S-1	0.0058	309	3.0	1.3	57 125	−9.6%	9372	−18.8%
S-2	0.0052	312	3.2	1.3	63 193	0.0%	11 549	0.0%
S-3	0.0052	322	2.8	1.3	67 109	6.2%	13 041	12.9%
S-4	0.0051	311	2.8	1.4	63 468	0.4%	11 966	3.6%
S-5	0.0052	323	2.7	1.3	63 027	−0.3%	13 198	14.3%
S-6	0.0056	310	2.6	1.4	60 611	−4.1%	14 559	26.1%
S-7	0.0057	313	2.2	1.3	63 118	−0.1%	17 147	48.5%
S-8	0.0054	311	1.9	1.3	68 094	7.8%	17 166	48.6%
S-9	0.0056	305	1.3	1.2	60 105	−4.9%	13 260	14.8%
Average					62 872			

Comparing the stiffness of the specimens shows that their elastic stiffness values were almost the same, while their plastic stiffness values were quite different at approximately 18%–27% of the elastic stiffness values.

4 Discussion

4.1 Effect of loading amplitude range

Comparing the strength and deformation capacities of specimens S-1 and S-2, which were subjected to the cyclic load of a different amplitude range as listed in Table 4, it can be seen that the bearing capacity of specimen S-1 endured a larger load amplitude than that of specimen S-2 by 6.7% (the average value of M_u in the positive cycle and negative cycle is taken as the connection bearing capacity), and their deformation capacities are almost the same, which indicates that the effects of the load amplitude range on specimen strength and deformation capacity are not obvious. The hardening stiffness of S-1 was smaller than S-2 by 18.8% as listed in Table 5, indicating a certain influence of load amplitude range on the connection hardening extent.

4.2 Effects of loading history and peak load

The effects of loading history and peak load on connection bearing and deformation capacity were studied by analyzing the performance of specimens S-2–S-5. These four specimens were tested under various loading protocols which simulated the different earthquake conditions as listed in Table 6. The load on specimen S-2 simulated an earthquake varying gradually from weak to strong. The loads on S-3 and S-4 both simulated an earthquake growing stronger until reaching the first peak load, and then the emerging aftershock, finally reaching the maximum amplitude which represents a severe

earthquake, while the first peak load values in the loading history for these two specimens were different. For specimens S-4 and S-5, the first peak load values were the same, specimen S-4 was loaded to peak value step by step, while specimen S-5 was loaded to peak value directly.

1. Effects of peak load value and appearing time

The bearing capacity and the maximum rotation of these four specimens (S-2–S-5) are close to one another as listed in Table 4. The skeleton curves of these four specimens are compared, and appear to be almost the same (Fig. 6).
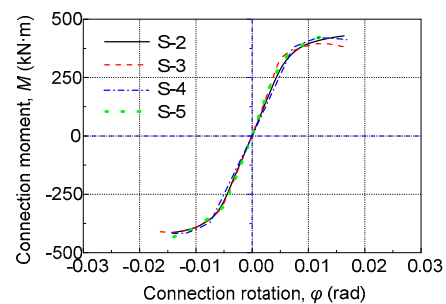

Fig. 6 Comparison of skeleton curves of S-2–S-5

Specimens S-2, S-4, and S-5 reached bearing capacity at the stage of first peak load, while specimen S-3 attained bearing capacity when the penultimate stage of load was applied, reaching its end state before the maximum load had been achieved, which indicates that the accumulated damage lead to the weakening of the specimen's performance. Specimen S-4 reached its end state just at the first peak load, and its bearing capacity decreased thereafter, which indicates that the medium seism (S-3) and the strong seism (S-4) accelerate the specimen damage process. Comparing the performances of specimens S-3 and S-4 in this test, the influence of peak load value does not appear to be obvious. From the damage process analysis of specimens S-7 and S-8, which were tested under a CA load, it can be seen that for the specimens

Table 6 Comparison of the loading factors between specimens

Specimen	Peak value	Peak load appearing time	Strength degradation	Corresponding earthquake condition
S-2	$2\delta_y^+$	The last stage of plastic	Progressive	Weak-strong
S-3	$1.5\delta_y$	The third stage of plastic	Progressive	Weak-medium-weak-strong
	$2\delta_y^+$	The last stage of plastic	Progressive	
S-4	$2\delta_y$	The fourth plastic stage	Progressive	Weak-strong-weak-strong
	$2\delta_y^+$	The last stage of plastic	Progressive	
S-5	$2\delta_y$	The first stage of plastic	Sudden	Strong-weak-strong
	$2\delta_y$	The last stage of plastic	Progressive	

Note: $2\delta_y^+$ is the loading amplitude when specimen failure occurs

subjected to loads with amplitudes of 22.5 mm and 26.25 mm, obvious damage started to appear after enduring 10 cycles. Specimen S-4 endured two more cycles at these two load stages than specimen S-3 did, so damage distinctive to these two specimens is not obvious. Therefore, the effect of load amplitude on specimen bearing capacity needs certain accumulated hysteric cycles to manifest.

2. Effect of peak load onset time

Comparing the deformation capacity and test phenomena of specimen S-5 with that of the other specimens, it can be observed that when S-5 was subjected to the peak load (30 mm) for the second time, the specimen completely fractured at the first cycle, while the other specimens endured two cycles and were subsequently loaded by 33.75 mm, which shows the worst deformation of specimen S-5 at the later stage of loading. The bearing capacity of specimen S-5 decreased to 217 kN and 172 kN in the last two cycles of load with an amplitude of 26.25 mm as shown in Fig. 7, and the beam flange cracked showing the obvious damage. In contrast, the bearing capacity of specimen S-4 was 259 kN and −255 kN in the last two cycles of the load with the same amplitude, which reflects the slow damage process. Therefore, the load type of burst strong seism applied to specimen S-5 is detrimental for the connection performance. Some conclusions can be drawn based on the analysis above:

(1) When specimens are subjected to the load with the same amplitude and cycle numbers, the influence of peak load onset time on their bearing capacity is small. Specimens reach their ultimate capacity at the first peak load, and the specimens' bearing capacity decreases gradually thereafter.

(2) The effect of peak load values on specimen performance has a close relationship with the number of load cycles; if the cyclic number is small, the influence is small. The bursting peak load is more detrimental to the connection performance than the progressive loading.

4.3 Effect of loading amplitude

In order to validate the ultra-low cycle fatigue (ULCF) characters of beam-to-column connection under plastic cyclic loading, and provide reference for the investigation under variable amplitude loading, specimens S-6–S-9 were treated with CA load with different loading amplitudes. It can be seen from

Table 4 that the specimen strength decreases with the decreasing loading amplitude. Apparently, the specimen tested under a load with a smaller amplitude entered the inelastic phase repeatedly and was damaged without taking full advantage of the material strengthening effect.

5 Damage analysis of beam-to-column connection

5.1 Connection damage process

Based on damage mechanics and previous research (Xiong, 2011), the reduced bearing capacity and the stiffness of the connection after damage are calculated by Eq. (2) as follows, and the connection damage index D can be obtained accordingly.

$$M_D = M_u(1 - D). \tag{2}$$

In this study, the bearing capacity of specimens S-6–S-9 subjected to a CA load is taken as the nondestructive moment resisting capacity M_u, and the connection bearing capacity M_D of each specimen is normalized by dividing M_u at every corresponding loading stage. Fig. 7 shows the normalized curves of the bearing capacity versus the cycle numbers, which exhibits the damage evolution process of the connections. The positive or negative sign represents the half cycle within which the bottom flange or the top flange is in tension, respectively.

5.2 Connection damage features

From the analysis of the damage evolution process of the specimens, some features of connection damage can be observed as follows:

(1) The progression of the damage accelerates. Once a crack has grown through the thickness of a beam flange, the bearing capacity of the connections being subjected to CA load progressively decreases, especially during the last two or three cycles of CA loading, and the damage correspondingly increases. Fig. 8 shows the curves of the damage index of each cycle versus accumulated plastic rotations, clearly demonstrating that the damage in each cycle increases during the last two or three cycles of loading. The damage indices at the inflexion point of the curve are approximate, showing the correlation between

damage development and the current accumulated damage. The larger the extent of the accumulated damage, the more damage will be caused by the plastic deformation of the same amplitude in the next cycle. That curve inflexion point is close to the point where the crack propagates through the beam flange,

which indicates the connection damage is mainly caused by the crack of metal in the plastic phase.

(2) The loading amplitude has an obvious effect on damage evolution. The damage evolution curves of the four CA specimens (tested under CA cyclic loads) are shown in Fig. 9. When the beam tip load
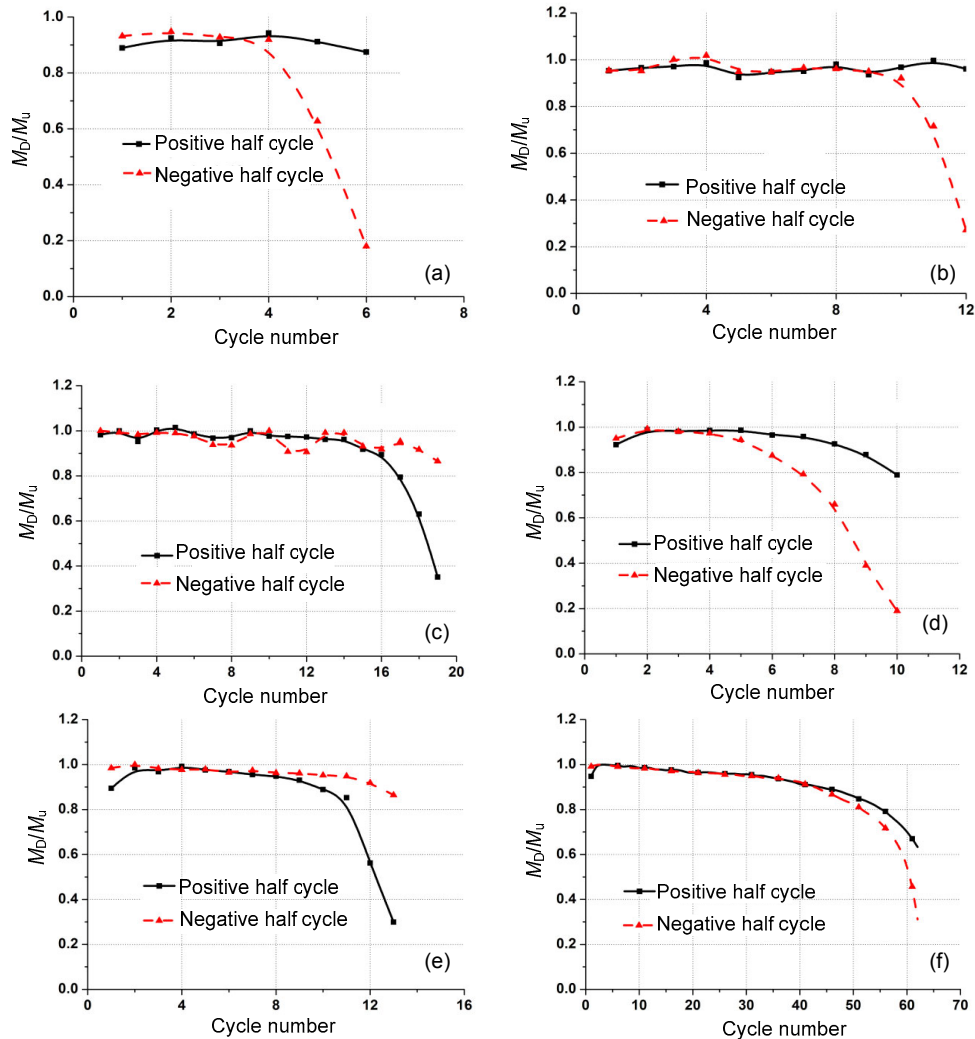

Fig. 7 Damage evolution process
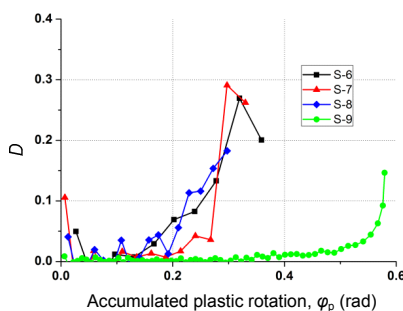(a) S-1; (b) S-2; (c) S-5; (d) S-6; (e) S-7; (f) S-9

Fig. 8 Curves of damage within each cycle versus accumulated plastic rotation under constant amplitude loads
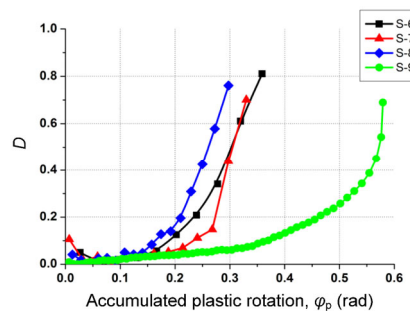
Fig. 9 Curves of damage versus accumulated plastic rotation under constant amplitude loads

amplitude exceeds $1.5\delta_y$ (for specimens S-6–S-8), the damage to the connections becomes evident. When the load amplitude is below this value (for specimen S-9), the damage caused under ultra-low cycle loading is negligible and can be ignored.

(3) The damage process curves of each specimen are approximate to the power function. Power function ax^b is adopted to fit the tested results as shown in Fig. 10. Fitting parameters are listed in Table 7. The fitting results show good agreement with test data, which indicates the power function is reliable for describing the course of the damage.

5.3 Validation of connection damage evolution equation

1. Linear cumulative damage evolution equation

The linear cumulative damage law is a commonly used damage model in the field of low cycle or ultra-low cycle fatigue. Based on the Miner linear damage assumption, the influence of the sequence of CA cyclic load is not taken into consideration. The total damage is obtained by adding the damage caused by each load with the same amplitude linearly. The damage corresponds to the specific load amplitude and can be calculated by

$$D_i = \frac{1}{N_{fi}}, \tag{3}$$

where N_{fi} denotes the cycle numbers of CA load with amplitude i. The damage caused by cyclic loads with different amplitudes is added linearly to calculate the damage of a specimen subjected to VA load as

$$D = \sum_{i=1}^{N} \frac{1}{N_{fi}}. \tag{4}$$

Table 7 Fitting parameters of damage process curves

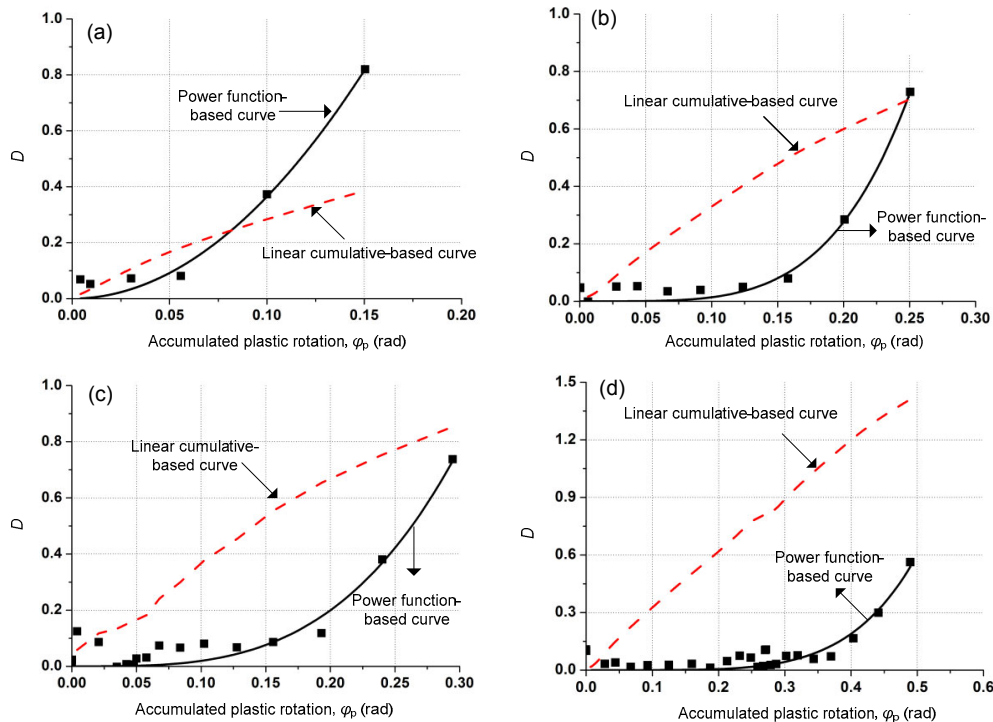| Specimen	a	b	R^2
S-1	35.4	1.98	0.9798
S-2	280.6	4.30	0.9735
S-3	44.1	3.35	0.9270
S-4	21.7	5.18	0.8685
S-5	310.4	5.09	0.9878
S-6	24.2	3.29	0.9924
S-7	420.5	5.76	0.9546
S-8	58.0	3.56	0.9928
S-9	4.3	3.88	0.9421
Average	133.24	4.04	
COV*	1.19	0.29	

* COV: coefficient of variance

Fig. 10 Damage evolution curves obtained by linear and power functions under VA loads
(a) S-1; (b) S-2; (c) S-3; (d) S-4

The damage evolution curves of the VA loaded specimens obtained by this linear assumption based model and the corresponding test results are shown in Fig. 10. The damage process produced by this model is quite different from the test results, so the linear cumulative damage law is not suitable for simulating the bending moment connection damage process.

2. Power function damage evolution equation

The accelerating rate of damage progression can be embodied by the power function-based damage law according to the previous analysis. The macro connection damage evolution equation is

$$D_i = \left(\frac{\varphi_{pi}}{\varphi_u - \varphi_y} \right)^c, \qquad (5)$$

where φ_{pi} represents the plastic rotation of every half cycle, φ_u represents the ultimate rotation of a connection subjected to monotonic load, and φ_y denotes the connection rotation at yield point. Combined with the concept of Miner linear cumulative damage, the damage can be expressed by the linear combination of the power function-based model as

$$D = \sum_{i=1}^{N} \left(\frac{\varphi_{pi}}{\varphi_u - \varphi_y} \right)^c. \qquad (6)$$

The test results of connection damage regressed by Eq. (6) are shown in Fig. 10, and the fitting parameter c is given in Table 8.

3. Modified Park-Ang combination model

Park and Ang (1985) proposed a damage evolution model combining the displacement and energy index as

$$D = \frac{\delta_{max}}{\delta_u} + \frac{\beta}{F_y \delta_u} \int dE', \qquad (7)$$

where δ_{max} is the maximum deformation under cyclic loading, δ_u is the ultimate deformation under monotonic loading, F_y is the yield strength, $\int dE'$ is cumulative dissipated energy, and β is a constant. In this model, displacement and energy are combined linearly.

The Park-Ang model can be modified to the expression of exponent function as

$$D = \left(\frac{\varphi_{max} - \varphi_y}{\varphi_u - \varphi_y} \right)^c + \beta \sum_{i=1}^{N} \left(\frac{\varphi_{pi}}{\varphi_u - \varphi_y} \right)^c, \qquad (8)$$

where the constant parameter β is taken as 0.23 according to the previous study (Xiong, 2011), and the parameter c is regressed by the test data obtained in this study. The fitting results are listed in Table 9.

Table 8 Fitting results of power function damage evolution model

Specimen	c	D
S-1	8.08	0.82
S-2	7.74	0.73
S-3	7.07	0.73
S-4	7.84	0.56
S-5	4.57	0.65
S-6	6.75	0.81
S-7	4.48	0.70
S-8	3.17	0.76
S-9	2.84	0.69
Average	5.84	
Standard deviation	2.08	
COV	0.36	

Table 9 Fitting results of modified Park-Ang damage evolution model

Specimen	c	D
S-1	5.04	0.82
S-2	5.80	0.73
S-3	4.76	0.73
S-4	6.80	0.56
S-5	3.12	0.65
S-6	4.39	0.81
S-7	3.00	0.70
S-8	2.12	0.76
S-9	2.07	0.69
Average	4.12	
Standard deviation	1.65	
COV	0.40	

The damage evolution curves for some of the specimens obtained by Eqs. (6) and (8) are compared in Fig. 11. The damage evolution curves obtained by these two models are approximate. The fitting results show that these two models are more suitable for simulating the damage process for specimens S-1–S-3, which were subjected to variable amplitude load, compared with CA loading specimens S-7–S-9

as shown in Fig. 11. However, the calibration for the parameters of these models is all dependent on test data regression; thus, a more general and accurate damage evolution model needs to be established.

5.4 Damage mechanism and ductile fracture-based damage evolution equation

Based on the analysis above, for a connection designed with the philosophy of strong column-weak beam, the connection damage is mainly caused by a crack in the metal in the plastic phase at the beam end, and the damage course is the crack process of the beam flange at the beam end. Skallerud and Zhang

(1997) have demonstrated that fatigue and tensioned ductile cracks are the major causes for crack development in these types of connections.

1. Metal fatigue theory

According to the Manson-Coffin relationship and Paris equations, which describe fatigue crack propagation, Solomon (1972) and Krawinkler and Zhorei (1983) proposed the relationship between crack length and connection cycle numbers under CA loads (Xiong, 2011):

$$\frac{\mathrm{d}a}{\mathrm{d}N} = \alpha a (\Delta\varepsilon_\mathrm{p})^{\beta}, \tag{9}$$
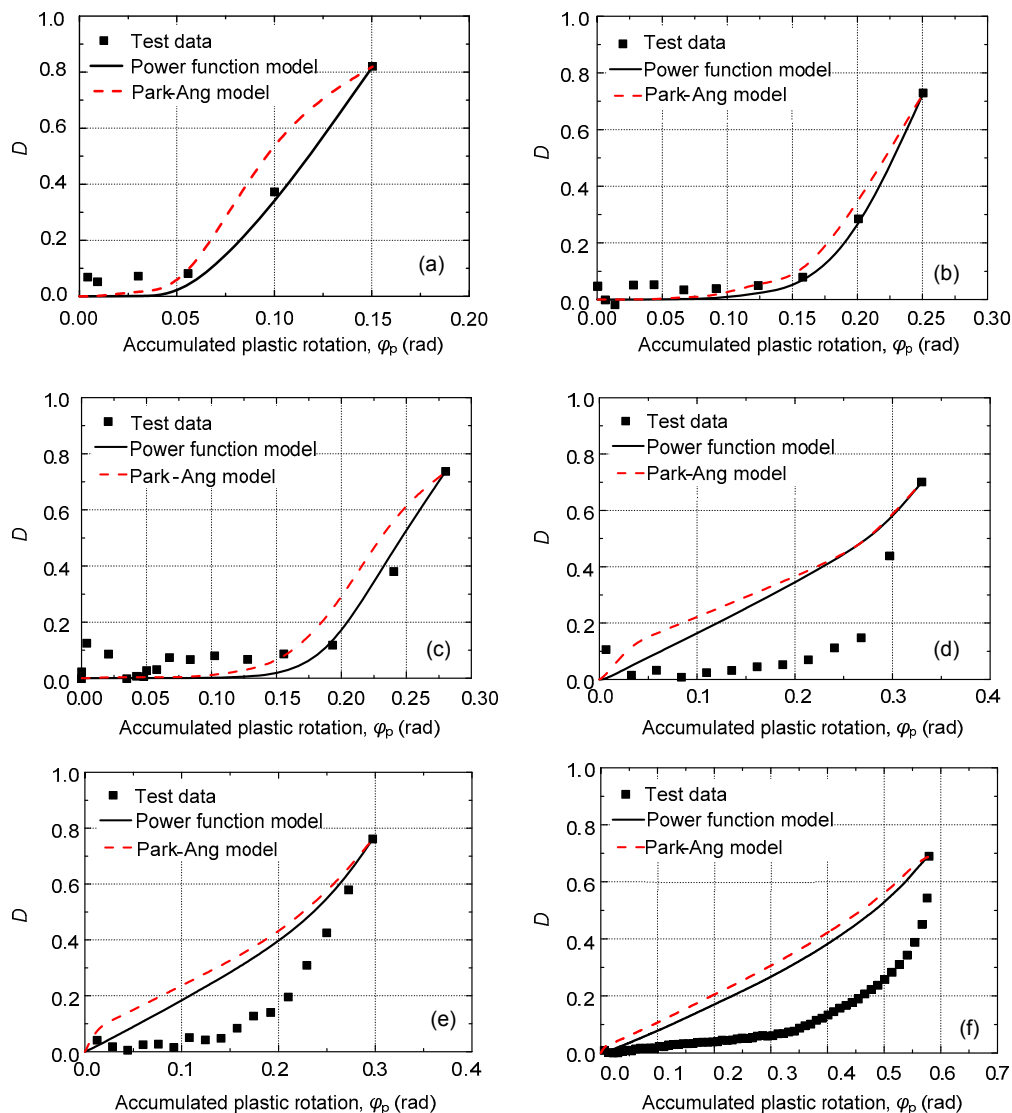

Fig. 11 Comparison between power function model and modified Park-Ang model
(a) S-1; (b) S-2; (c) S-3; (d) S-7; (e) S-8; (f) S-9

where a is the crack length, N is the cycle number, $\Delta\varepsilon_p$ denotes the half of the amplitude range of plastic strain, α and β are the material property related parameters.

2. Metal ductile fracture theory

Under cyclic loading, when the stress amplitude exceeds the material yield strength, the material turns into plastic repeatedly, leading to the initiation of ductile fractures in metal. It is assumed that ductile fracture initiation results from void growth and coalescence, which is related to plastic strain and stress triaxialities surrounding the void. A brief review of the cyclic void growth model (CVGM) developed by Kanvinde and Deierlein (2004) based on the previous work of Rice and Tracey (1969) is given here. It is postulated that voids expand and shrink under cyclic loading due to altering excursions of positive and negative mean stresses or stress triaxialities. The driving force behind void growth is the cumulative tension plastic strain; ductile fracture initiation occurs when the void reaches a critical size. For a single spherical void in an infinite continuum, the void growth rate under monotonic tensile loading can be expressed as (Kanvinde and Deierlein, 2004; Wang *et al.*, 2011; Liu *et al.*, 2016)

$$\mathrm{d}r \,/\, r = C\,\mathrm{e}^{1.5T_R}\,\mathrm{d}\varepsilon_p, \qquad (10)$$

where r is the instantaneous void radius; $T_R=\sigma_m/\sigma_e$ is the stress triaxiality (ratio of mean stress σ_m to effective stress σ_e); C is a material constant; $\mathrm{d}\varepsilon_p$ is the incremental equivalent plastic strain. Therefore, a ductile fracture caused by void growth is proportional to $\mathrm{e}^{1.5T_R}\,\mathrm{d}\varepsilon_p$, and the ductile strain ε_p^* is defined as the index to describe the ductile fracture accordingly

$$\varepsilon_p^* = \mathrm{e}^{1.5T_R}\,\varepsilon_p. \qquad (11)$$

Under cyclic reverse loading, when the triaxiality is positive, the void expands under plastic straining, and if it is negative, the void shrinks. The magnitude of triaxiality T_R and the equivalent plastic strain govern the rate of void growth or shrinkage. T_t and T_c represent the stress triaxiality when tensioned and compressed, respectively. Integrating Eq. (10) over tensile and compressive loading excursions respectively, the term ε_p^* during cyclic loading can be expressed as

$$\varepsilon_p^* = \int_0^t [\mathrm{e}^{1.5T_t}\varepsilon_t(t) - \mathrm{e}^{|1.5T_c|}\varepsilon_c(t)]\mathrm{d}t,$$
$$\mathrm{e}^{1.5T_t}\varepsilon_t(t) - \mathrm{e}^{|1.5T_c|}\varepsilon_c(t) > 0, \qquad (12)$$

where ε_t and ε_c represent the strain when tensioned and compressed, respectively.

3. Ductile fracture based damage evolution equation for connection

Studying the connection damage behavior together with the fracture mechanism, the evolution of connection damage can be captured by investigating crack development in beam-to-column connections. To relate the ductile fracture micro mechanism to the macro connection fracture analysis, it was assumed that the initial defect distributed uniformly in the beam flange at the beam end. The effect of crack location in the beam flange was not taken into consideration in this study. The initial crack can be presumed to be the surface crack of the beam flange according to the equal defect area. Based on the fundamental assumptions of damage mechanics, crack propagation through the thickness of the beam flange can be regarded as a reduction in the effective area of the beam flange. Therefore, the damage process can be obtained by analyzing crack propagation. Considering the main driving force of crack growth is the ductile strain range $\Delta\varepsilon_p^*$ within each cycle, the crack growth rate expression is rewritten as

$$\frac{\mathrm{d}a}{\mathrm{d}N} = \alpha a(\Delta\varepsilon_p^*)^\beta. \qquad (13)$$

As the stress triaxiality is related to the geometries of a specimen, numerical computation is needed to calculate the triaxiality for a connection with complicated geometries. Previous study indicates that the theoretical value of triaxiality can be taken as 1/3 and $-1/3$ when a beam flange is subjected to tension and compression, respectively (Xiong, 2011). Therefore, Eq. (12) can be simplified as

$$\varepsilon_p^* = \mathrm{e}^{1.5T_R}\int_0^t [\varepsilon_t(t) - \varepsilon_c(t)]\mathrm{d}t, \ \varepsilon_t(t) - \varepsilon_c(t) > 0. \quad (14)$$

The summation term of the equation can be defined as effective plastic strain ε_{EPS}:

$$\varepsilon_{EPS} = \int_0^t [\varepsilon_t(t) - \varepsilon_c(t)]\mathrm{d}t. \qquad (15)$$

When stress triaxiality distributes uniformly, the effective plastic strain range $\Delta\varepsilon_{EPS}$ is the key factor influencing the connection fracture. Therefore, Eq. (13) can further be simplified with the term of $\Delta\varepsilon_{EPS}$:

$$\frac{\mathrm{d}a}{\mathrm{d}N} = \alpha a \mathrm{e}^{1.5T_R\beta}(\Delta\varepsilon_{EPS})^{\beta}. \tag{16}$$

The growth in crack length in each cycle under CA loads can be obtained by integration of Eq. (16):

$$a_{i+1} = a_i \mathrm{e}^{\alpha \mathrm{e}^{1.5T_R\beta}(\Delta\varepsilon_{EPS})^{\beta}}. \tag{17}$$

Based on the assumption of a surface crack, the bearing capacity of the connection after a crack appears in the beam flange can be calculated as Fig. 12 shows. In this study, a beam flange that has completely fractured is regarded as being in its end state, and the plane-section assumption is adopted to calculate its ultimate strength.
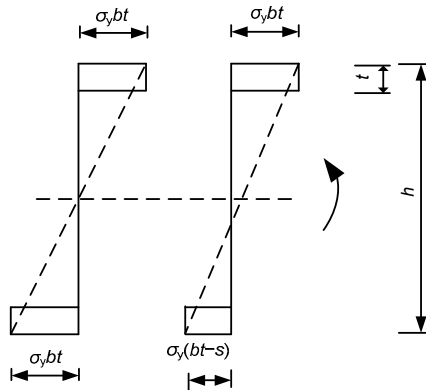

Fig. 12 Schematic of calculation for connection bearing capacity after flange crack

The bearing capacity of a connection with crack area s can be obtained approximately by

$$M_D = \sigma_y(bt - s)(h - t), \tag{17}$$

where b and t represent the beam flange width and thickness, respectively, h is the height of the beam section, and σ_y denotes the material yield strength. The crack area s can be obtained by integration of every crack length at different locations:

$$s = \int_0^b a(x)\mathrm{d}x. \tag{18}$$

The relationship between connection damage and crack length within each cycle can be quantified as

$$D_i = \int_0^b \frac{a(x,i)}{bt}\mathrm{d}x. \tag{19}$$

This equation is suitable for the CA loading, and it can be employed approximately in the situation of variable loading according to the Miner linear cumulative concept. Compared with the power function model and the Park-Ang model mentioned above, this fracture mechanism-based model has some advantages as follows:

1. This model is based on fatigue damage mechanics and the ductile fracture mechanism, and effective plastic strain is adopted as the damage evolution index in this model. The parameters of the model have definite physical meanings.

2. It can reflect the accelerating damage evolution of connection. By relating the damage of the current cycle to the crack length in last cycle, the effect of accumulated damage on damage development is described.

3. The different influence of tension and compression load on connection damage has been taken into consideration by adopting the effective plastic strain to evaluate the damage process, which better conforms to the practical damage mechanisms of metal material.

4. The effect of loading history is considered by including the accumulated damage of each cycle.

6 Conclusions

In order to investigate the damage behavior of beam-to-column connections in SMRFs during severe earthquakes, a series of tests were carried out on nine full scale specimens of connections, in which five specimens were tested under variable cyclic loading and four specimens were tested under constant cyclic loading. Based on the test results, three damage evolution models were validated, and a model that captures the underlying mechanisms of damage was proposed according to fatigue fracture mechanics. The following conclusions can be drawn:

1. In the connection tests, the cracks initiated from the toes of the WAHs in the beam flanges and

then propagated through the thickness of the beam flanges just beneath the WAHs. A total of six specimens fractured completely through the beam top flanges through the toe of the WAH and the other three (i.e., specimens S-3, S-5, and S-7) fractured across the beam bottom flanges.

2. The effects of loading amplitude, loading history, and peak load on the connection damage were analyzed. The test results indicate that when the weld quality is guaranteed, connection fractures are most likely to initiate from the WAH, and load amplitude range has less impact on the connection damage behavior. The influence of loading history is closely related to the peak load cycle numbers, and the bursting strong peak load is very detrimental to the connection.

3. The relationship between connection damage and its bearing capacity was established; the character of connection damage was analyzed according to the damage process. It is demonstrated that damage to the connections accelerated in the process of cyclic loading, which is related to the load amplitude and cumulative damage during loading. Power function proved to be reliable for describing the development of the damage.

4. Three commonly used damage evolution models were calibrated and validated by the test data. The comparison between these models and the data revealed that the power function-based model and the Park-Ang combination model are suitable for simulating a connection under variable amplitude cyclic loading. However, these models are dependent on test data regression to describe the damage process, and the parameters of each model do not have definite physical meanings, so a damage mechanism-based model needs to be established.

5. The effective plastic strain was developed to quantify the damage process with reference to the nature of the damage caused to connections under cyclic reverse loading. It was defined by subtracting the compressed strain, which leads to the crack enclosure, from the tensile plastic strain, and variations in the microstructures of the material during the cyclic loading process were taken into consideration. Finally, based on the damage mechanism and ductile fatigue fracture mechanics, a damage evolution equation which adopts the index of effective plastic strain was proposed.

References

Anderson, J.C., Duan, J., Xiao, Y., *et al.*, 2002. Cyclic testing of moment connections upgraded with weld overlays. *Journal of Structural Engineering*, **128**(4):509-516. http://dx.doi.org/10.1061/(ASCE)0733-9445(2002)128:4(509)

BS (British Standards), 2005. Eurocode 3: Design of Steel Structures: Part 1-1: General Rules and Rules for Buildings, BS EN 1993-1-1. BS, London, UK.

Chen, T., 2007. Extremely Low Cycle Fatigue Assessment of Thick-walled Steel Piers. PhD Thesis, Nagoya University, Japan.

Chi, B., Uang, C.M., 2002. Cyclic response and design recommendations of reduced beam section moment connections with deep columns. *Journal of Structural Engineering*, **128**(4):464-473. http://dx.doi.org/10.1061/(ASCE)0733-9445(2002)128:4(464)

Dexter, R.J., Melendrez, M.I., 2000. Through-thickness properties of column flanges in welded moment connections. *Journal of Structural Engineering*, **126**(1):24-31. http://dx.doi.org/10.1061/(ASCE)0733-9445(2000)126:1(24)

El-Tawil, S., Mikesell, T., Vidarsson, E., *et al.*, 1998. Strength and Ductility of FR Welded-bolted Connections. SAC Report No. 98-01, Washington, USA.

Fisher, J.W., Dexter, R.J., Kaufmann, E.J., 1995. Fracture Mechanics of Welded Structural Steel Connections. SAC Report No. 95-09, Washington, USA.

Kanvinde, A.M., Deierlein, G.G., 2004. Micromechanical Simulation of Earthquake-induced Fracture in Steel Structures. Blume Center TR 145. Stanford University, Stanford, USA.

Krawinkler, H., Zhorei, M., 1983. Cumulative damage in steel structures subjected to earthquake ground motions. *Computers & Structures*, **14**(1-4):531-541. https://doi.org/10.1016/0045-7949(83)90193-1

Kuwamura, H., 1998. Fracture of steel during an earthquake–state-of-the-art in Japan. *Engineering Structures*, **20**(4-6): 310-322. http://dx.doi.org/10.1016/S0141-0296(97)00030-8

Kuwamura, H., Yamamoto, K., 1997. Ductile crack as trigger of brittle fractures in steel. *Journal of Structural Engineering*, **123**(6):729-735. http://dx.doi.org/10.1061/(ASCE)0733-9445(1997)123:6(729)

Kuwamura, H., Takagi, N., 2004. Similitude law of prefracture hysteresis of steel members. *Journal of Structural Engineering*, **130**(5):752-761. http://dx.doi.org/10.1061/(ASCE)0733-9445(2004)130:5(752)

Li, H.Q., Ben, Q.G., Yu, Z.C., *et al.*, 2004. Analysis and experiment of cumulated damage of steel frame structures under earthquake action. *Journal of Building Structures*, **25**(3):69-74 (in Chinese).

Liu, X.Y., Wang, Y.Q., Xiong, J., *et al.*, 2016. Investigation on micromechanical fracture prediction model of high strength steel and its weld. *Journal of Building Structures*, **37**(6):228-235 (in Chinese).

MOHURD (Ministry of Housing and Urban-rural Development of the People's Republic of China), 2003. Code for Design of Steel Structures, GB50017-2003. MOHURD, China (in Chinese).

MOHURD (Ministry of Housing and Urban-rural Development of the People's Republic of China), 2010. Code for Seismic Design of Buildings, GB50011-2010. MOHURD, China (in Chinese).

Nip, K.H., Gardner, L., Davies, C.M., *et al.*, 2010. Extremely low cycle fatigue tests on structural carbon steel and stainless steel. *Journal of Constructional Steel Research*, **66**(1):96-110.
http://dx.doi.org/10.1016/j.jcsr.2009.08.004

Park, A.J., Ang, H.S., 1985. Mechanistic seismic damage model for reinforced concrete. *Journal of Structure Engineering*, **111**(4):722-731.
http://dx.doi.org/10.1061/(ASCE)0733-9445(1985)111:4(722)

Rice, J.R., Tracey, D.M., 1969. On the ductile enlargement of voids in triaxial stress fields. *Journal of Mechanics and Physics of Solids*, **17**(3):201-217.
http://dx.doi.org/10.1016/0022-5096(69)90033-7

Saiprasertkit, K., Hanji, T., Miki, C., 2012. Fatigue strength assessment of load-carrying cruciform joints with material mismatching in low- and high-cycle fatigue regions based on the effective notch concept. *International Journal of Fatigue*, **40**:120-128.
http://dx.doi.org/10.1016/j.ijfatigue.2011.12.016

Sakano, M., Wahab, M.A., 2001. Extremely low cycle (ELC) fatigue cracking behaviour in steel bridge rigid frame piers. *Journal of Materials Processing Technology*, **118**(1-3):36-39.
http://dx.doi.org/10.1016/S0924-0136(01)00857-3

Shen, Z.Y., Shen, S., 2002. Seismic analysis of steel tall structures with damage cumulation and fracture effects. *Journal of Tongji University*, **30**(4):393-398 (in Chinese).

Shi, W.L., Xiao, Y., Li, G.Q., *et al.*, 2008. Pseudo-dynamic tests on composite joints with flush end plate connections. *Earthquake Engineering and Engineering Vibration*, **28**(6):124-133 (in Chinese).

Shi, Y.J., Ao, X.L., Wang, Y.Q., *et al.*, 2009. Experimental study on the seismic performance of beam-to-column composite connections in medium-high strength steel frame structures. *China Civil Engineering Journal*, **42**(4):48-54 (in Chinese).

Skallerud, B., Zhang, Z.L., 1997. A 3D numerical study of ductile tearing and fatigue crack growth under nominal cyclic plasticity. *International Journal of Solids and Structures*, **34**(24):3141-3161.
http://dx.doi.org/10.1016/S0020-7683(96)00137-0

Solomon, H.D., 1972. Low-cycle fatigue crack-propagation in 1018 steel. *Journal of Materials*, **7**(3):299-306.

Su, D., 2005. Seismic Behavior of Beam-column Connections in Steel Structure with Composite Effect. PhD Thesis, Tsinghua University, Beijing, China (in Chinese).

Tateishi, K., Hanji, T., 2004. Low cycle fatigue strength of butt-welded steel joint by means of new testing system with image technique. *International Journal of Fatigue*, **26**(12):1349-1356.
http://dx.doi.org/10.1016/j.ijfatigue.2004.03.016

Toyoda, M., 2002. Properties of Steel Structures Damaged in Hanshin-Japan and Northridge-USA Earthquake. Seminar Notes. Dokuz Eylul University, Izmir, Turkey.

Wang, J.M., Chen, L.Z., 2005. Damage detection of frames using the increment of lateral displacement change. *Journal of Zhejiang University-SCIENCE A*, **6**(3):202-212.
http://dx.doi.org/10.1631/jzus.2005.A0202

Wang, Y.Q., Zhou, H., Shi, Y.J., *et al.*, 2011. Fracture prediction of welded steel connections using traditional fracture mechanics and calibrated micromechanics based models. *International Journal of Steel Structures*, **11**(3):351-366.
http://dx.doi.org/10.1007/s13296-011-3010-2

Xiong, J., 2011. Research on the Damage Behavior and Calculation Model of Welded Connections in Steel Frames under Earthquakes. PhD Thesis, Tsinghua University, Beijing, China (in Chinese).

中文概要

题　目：钢框架梁柱节点在强震作用下的损伤性能研究

目　的： 钢框架焊接梁柱节点在地震作用下往往容易产生脆性裂纹，裂纹的发展和损伤累积将导致节点延性降低，发生脆性断裂。本文旨在探究节点在地震往复荷载作用下的损伤性能，分析其主要影响因素，提出有效的损伤评估模型，为后续节点损伤数值模拟提供基础，为钢框架的抗震设计提供参考。

创新点： 1. 通过足尺节点试验，分析加载幅值、加载历程和荷载峰值对节点损伤性能的影响；2. 基于试验结果，标定并验证3种经验损伤演化模型，提出基于疲劳断裂力学的节点损伤评估模型。

方　法： 1. 通过对9个足尺梁柱节点试件开展往复加载试验，包括5种变幅加载制度及4种常幅加载制度，分析加载幅值、加载历程和荷载峰值对节点损伤性能的影响；2. 基于试验结果，根据节点损伤特点，在能量模型基础上，推导并拟合适用于节点循环加载的双参数损伤演化方程，并与其他模型进行比较，以验证其准确性；3. 结合疲劳和延性断裂理论，依据损伤机理，定义"有效塑性应变"量化损伤过程，并以疲劳裂纹发展公式为基础，推导适用于计算在极低周循环荷载下节点损伤过程的损伤演化方程。

结　论： 1. 加载跨幅对节点性能影响较小；加载历程的影响与历程中峰值位移循环次数密切相关；突发性的强峰值对节点造成的损伤最大。2. 节点损伤过程为幂函数形式；通过比较表明，在能量模型基础上推导出的适用于节点循环加载的双参数损伤演化方程，相对于单参数线性模型，能够更准确模拟节点在极低周循环下的损伤过程。3. 基于疲劳断裂力学理论的损伤演化方程物理意义明确，能够描述节点循环损伤试验中所表现出的加速损伤及"损伤拐点"特征。

关键词： 梁柱节点；往复荷载；节点试验；损伤机理；延性断裂